Free Spectral Range Matched Interrogation Technique for Wavelength Demodulation of Fiber Bragg Grating Sensors

by

Somayyeh Rahimi

A thesis
presented to the University of Waterloo
in fulfillment of the
thesis requirement for the degree of
Master of Applied Science
in
Electrical and Computer Engineering
Waterloo, Ontario, Canada, 2009

I hereby declare that I am the sole author of this thesis. This is a true copy of the thesis, including any required final revisions, as accepted by my examiners.

I understand that my thesis may be made electronically available to the public.

Abstract

Free Spectral Range Matched Interrogation (FSRMI) technique for wavelength demodulation of fiber Bragg grating sensors. We designed and tested a new wavelength demodulation system based on free-spectral-range-matched interrogation which employs a tunable fiber Fabry-Perot interferometer (FPI) and a multi-channel bandpass filter. This technique was deployed to test fiber Bragg gratings (FBG), long period gratings (LPG) and tilted fiber Bragg gratings (TFBG). In the experimental setup, a broadband source launches light into a fiber Bragg grating under test and the reflection/transmission spectrum is fed into a tunable FPI. By tuning an external bias applied to the FPI, the transmission spectrum of FPI scans over a wavelength range. The input optical signal is therefore selectively passed through the FPI and then fed into a four-channel bandpass filter followed by four photodetectors. The optical signal is converted to electrical signal by the photodiodes and is acquired by a data acquisition system. Since a bandpass filter with four channels are used in this interrogation system it can scan four distinguished wavelength ranges simultaneously and thus the scan rate is four time faster. We used this setup for doing some temperature and strain sensitivity measurements on some fiber gratings. Strain sensitivity measurements were done on FBG, TFBG and LPG and temperature sensitivity measurements were performed on TFBG. The strain and temperature sensitivity coefficients of these fiber Bragg grating sensors were obtained from experimental data. Our results show the potential of the integration of the FSRMI system with fiber Bragg gratings for temperature and strain multiple-sensor arrays with high sampling speed and high accuracy.

Acknowledgements

First and foremost I would like to express my sincere gratitude to my supervisor Professor Dayan Ban for his guidance and support throughout my research. His patience and positive attitude for managing the research and solving the problems have made this research possible.

Special thanks go to my supervisor Dr. George Xiao in Institute for Microstructural Sciences of National Research Council of Canada for his guidance for completing the experiments. I also would like to appreciate the assistance of Photonics System's group of Institute for Microstructural Sciences specially Dr. Frank Zhang and Ping Zhao.

I thank Professor Amir Hamed Majedi and Professor Siva Sivoththaman for their valuable comments and feedbacks on my thesis.

I have been lucky to have met a remarkable group of friends and colleagues in Waterloo. I would like to thank Saiedeh Razavi, Parisa Bohlouli, Saeed Fathololoumi, Andy Stumpf and Afsaneh Nabifar. Their contributions are many and I hope that the friendship bonds continue to strengthen in the future.

My love and affection to my family, my dear mother and father and my sisters and brother. Without their life long support I could not have come this far and left the sight of shore.

Dedication

This thesis is dedicated to my dear Mother and Father.

Contents

List of Tables

List of Figures

Chapter 1

Introduction

The development of fiber optic sensors that are fabricated based on fiber gratings has attracted interests as a displacement for conventional electro-mechanical sensor systems. They have advantages over the conventional sensing systems, such as their electrically passive operation, electro-magnetic interference (EMI) immunity, high sensitivity and multiplexing capabilities, where multi-parameters sensing is feasible. However, it has been challenging for fiber grating sensors to compete with the well-developed electro-mechanical sensors. Part of the reason is because of the wavelength demodulation systems or interrogation systems that are needed to convert the change in the spectrum of the gratings to the change in environmental parameters such as temperature, pressure, displacement and humidity.

The process of the operation of the fiber grating sensors starts by analyzing their spectrum. The infrared light passes through gratings and based on the type of the grating, the reflection or transmission spectrum will be studied. Because of the wavelength coupling between core and cladding modes that occurs through the grating, some wavelengths are attenuated or enhanced which result in observing peaks or dips in the grating spectrum. Based on the variations in the environmental conditions the locations of these peaks or dips can shift to longer or shorter wavelengths. This change in wavelength can be converted to the variations in envi-

ronmental parameters by using interrogation systems. In order to be able to sense the smallest amount of variations in the measurands, the interrogation systems need to have high resolution and fast scanning rate.

The interrogation techniques are divided into two groups; active detection techniques and passive detection techniques. The former group refers to the detection schemes that do not use any electrical, mechanical or optical active devices and performed measurand monitoring by detecting optical power or by using linearly wavelength dependent devices. The later group usually involve tracking, scanning or modulating mechanism to monitor the spectrum shift of the fiber grating sensors. Although the active detection systems require more complex components and are slower compared to passive detection scheme, they show better resolution.

In this research we report the designing and developing of an active interrogation system based on using a tunable Fabry–Perot interferometer and a mechanical multi–channel bandpass filter. By tuning the voltage that is being applied to the Fabry-Perot interferometer, the spectrum of the interferometer is compared to that of the fiber grating at each tuning step. If they match, the wavelength is read and recorded. By doing these steps for the whole wavelength range, one can get the spectrum of the fiber grating sensor. The advantage of using this system is its ability for scanning multiple wavelength bands simultaneously by employing a mechanical multi-channel band-pass filter. This makes the scanning rate faster by n times where n is the number of channels of the band-pass filter. In order to test the system the coefficients of temperature and strain sensitivity of fiber Bragg grating (FBG), long period grating (LPG) and tilter fiber Bragg grating (TFBG) are measured. The results show an accuracy on the order of 10 pm for measuring the shift of the grating spectrum.

This thesis consists of five chapters. In the next chapter a review on the literature of fiber Bragg grating sensors and their interrogation technique is done. The third and fourth chapters contain the designing of the interrogation system that we used for doing measurements and the results of strain and temperature measure-

ments that are performed on fiber gratings. In the last chapter, the summary of the measurements and results are given.

Chapter 2

Theoretical and Technical Review

2.1 Fiber Optic Sensors

Over the past three decades and because of innovation and growth of opto–electronic and fiber optic communication, two main technologies have been developed: one of them is the fiber optic communication industry and the other one is the fiber optic sensor technology. The fiber optic communication has been implemented in products such as laser printers, bar code scanners and compact disc players. Their advantage are mainly providing high performance and very reliable telecommunication links. The fiber optic sensor technology has been proceeding by the development and mass production of opto–electronic components. Over the years the production of cost-effective and high quality components have made the fiber optics sensor technology to be a more serious replacement for the well–developed electro–mechanical sensors. Fiber optic sensors can be used for measuring variations in electric and magnetic fields, temperature, pressure, vibration, strain [1] and humidity [25]. Therefore they can be used in a wide variety of applications. The advantage of using fiber optic sensors in comparison to traditional electro–mechanical sensors can be listed as being light–weight, small–size, passive operation mode, environmental ruggedness and resistant to electro–magnetic interference.

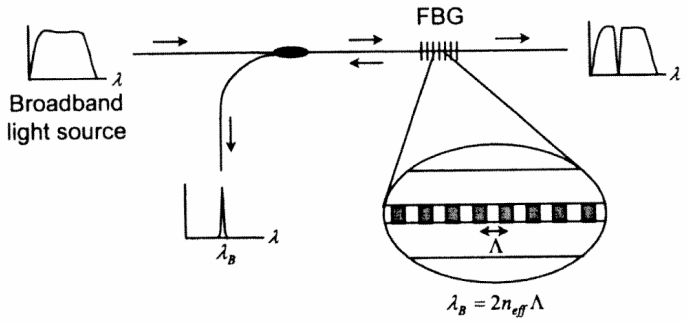

Figure 2.1: Principle of the fiber Bragg grating sensors

Fiber optic sensors can be divided into two separate groups of intrinsic sensors and extrinsic sensors. In the former the fiber itself acts as the sensing medium and so the propagating light never leaves the fiber, in contrast to the extrinsic sensors that the fiber merely acts as a light delivery and collection system. An example of the former fiber optic sensing method is the fiber Bragg grating sensors that are mostly used for sensing variations of strain and temperature. In this research we focus on the fiber Bragg gratings sensors, their fabrication methods and the interrogation techniques that are being used for measuring the shift in their spectrum due to change in the surrounding parameters.

2.2 Theory of Fiber Gratings

Fiber gratings can be categorized into periodic gratings and aperiodic gratings. Periodic gratings include fiber Bragg gratings (FBGs), long period fiber gratings (LPGs) and tilted fiber Bragg gratings (TFBGs). Aperiodic gratings include chirped fiber gratings and others. These gratings can be used in sensor heads or data–extracting systems. Figure 2.1 shows the principle of the FBG sensor. Light from a broadband spectrum source is launched into the Bragg grating sensor. Inside the fiber the optical wave is partially reflected from the grating. The coupling occurs between the incoming light and the light that is reflected back by the core

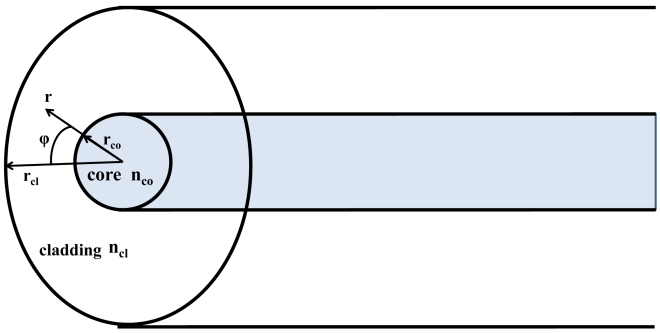

Figure 2.2: Cross-section of the fiber geometry considered here, showing the refractive indices and the radii of core and cladding.

and the cladding of the fiber. This gives rise to attenuation of light at some specific wavelengths in the transmission of the gratings. The attenuated wavelengths depend on the refractive indices of the core and cladding and the period of the gratings.

In order to have a better understanding of the the fiber grating sensor systems we will use the coupled–mode theory which is the most widely used method for the analysis of periodic media [3]. the guided optical fiber modes can be classified in two types. The first type are the core modes that are totally reflected at the core–cladding boundary and are confined inside the core region. The other are cladding modes that are totally reflected at the cladding–air boundary and are bounded in cladding and core regions. Figure 2.3 illustrates both modes. The interaction that we are going to consider occur mainly between the fundamental core mode HE_{11} or LP_{01} and the cladding modes of a step–index fiber. To keep the analysis clear and focus on mode interactions instead of calculating the modes themselves we assume a simple three layer step–index fiber geometry shown in figure 2.2. We are also assuming that $\Delta = \frac{n_1 - n_2}{n_1}$ is very small and therefore the linearly polarized

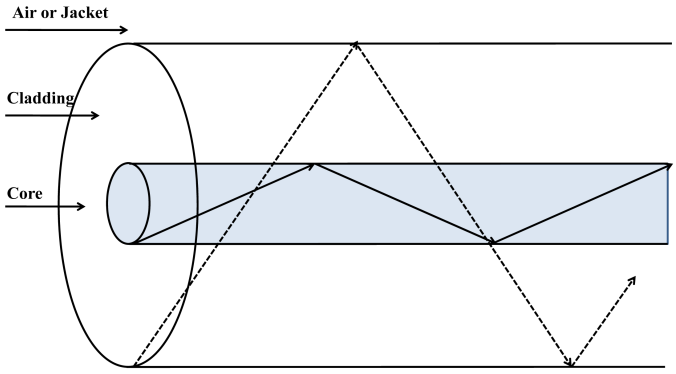

Figure 2.3: Optic illustration of the guided mode

(LP) approximation should be sufficient to describe a mode guided by the fiber core. This description will be used for finding the mode propagation constant. In particular the dispersion relation that we solve to obtain the LP_{01} mode effective index is:

$$V\sqrt{1-b}\frac{J_1(V\sqrt{1-b})}{J_0(V\sqrt{1-b})} = V\sqrt{b}\frac{K_1(V\sqrt{b})}{K_0(V\sqrt{b})} \tag{2.1}$$

where

$$V = \frac{2\pi r_{co}}{\lambda}\sqrt{(n_{co})^2 - (n_{cl})^2} \tag{2.2}$$

$$b = \frac{(n_{eff})^2 - (n_{cl})^2}{(n_{co})^2 - (n_{cl})^2} \tag{2.3}$$

where J_n is a Bessel function of the first kind; K_n a modified Bessel function of the second kind; V is the V–number of the fiber at wavelength λ and b is the normalized effective refractive index. The core refractive index, the cladding refractive index and the effective refractive index of the core are shown by n_{co}, n_{cl}, n_{eff} respectively. In the presence of perturbation along the fiber the optical modes can be coupled to one another. The main coupling directions can be determined as contra–directional or co–directional based on wether the traveling directions of modes coupled to each

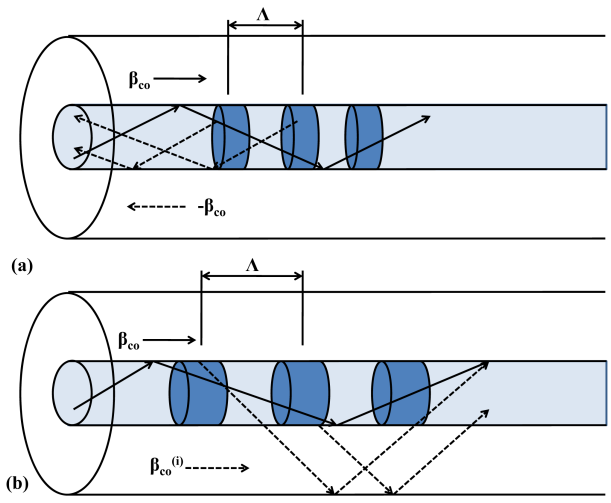

Figure 2.4: Illustration of mode coupling, (a) Contra–directional coupling, (b)co–directional coupling

other are opposite or the same. Based on the direction of the mode coupling, fiber gratings can be classified in two types. One type is a short period or reflection grating, where coupling occurs between modes traveling in opposite directions. The fiber Bragg gratings (FBG) and tilted fiber Bragg gratings (TFBG) belong to this category. The other type is a transmission grating, represented by long period gratings (LPG), where coupling occurs between modes traveling in the same direction [4].

An illustration of mode couplings is shown in figure 2.4. By means of refractive index perturbation, diffracted modes can be excited. For the diffracted mode to be built up constructively, each diffracted radiation from the series of the perturbation should be in–phase. Therefore the following equation must be satisfied:

$$\beta_i - (\pm\beta_d) = \frac{2\pi}{\Lambda} m \tag{2.4}$$

where β_i and β_d are the propagation constants for the incident and diffracted modes, Λ is the period of the grating and m stands for an integer number. The

minus sign behind the propagation constant describes the case where the mode propagates in the z–direction. The optical path difference between light diffracted from the adjacent grating positions should be an integer multiple of the wavelength for a resonant coupling of modes, as in the case of the constructive interference in dielectric multi–layers. In most cases first order diffraction is dominant and therefore m is assumed to be unit [5]. Thus the resonant wavelength for a single mode fiber can be written as:

$$\lambda = (n_{co} - (\pm n_{cl}))\Lambda \tag{2.5}$$

In the case of contra–directional coupling, the nominal Bragg wavelength of the core mode is given by:

$$\lambda = 2n_{co}\Lambda \tag{2.6}$$

When the core mode becomes coupled to the counter–propagating cladding mode, the n_{cl} is given by the effective refractive index of a cladding mode with a minus sign, which is possible in the case of strong Bragg gratings and blazed ratings [4]. In the case of co–directional coupling, the resonant wavelength for coupling between the core and cladding modes is given by:

$$\lambda = (n_{co} - n_{cl}^{i})\Lambda \tag{2.7}$$

where $n_{cl,eff}^{i}$ is the effective index of the i^{th} cladding mode. The differences in effective indices between the core and cladding modes are much smaller than unity and therefore the grating period for co–directional coupling at a given wavelength is much longer that that for contra–directional coupling.

2.3 Interrogation Techniques

Interrogators or demodulators in fiber grating sensor systems are the measurand–reading units that extract measurand information from the light signals coming from the sensor heads. The measurand is typically encoded spectrally and therefore the interrogators are usually meant to measure the wavelength shifts and convert the results to measurand data. Interrogation techniques can be classified in two categories; passive detection techniques and active detection techniques. The former are the devices that use passive electronic and optical components and the later are units that use active electronic and optical components. Our focus in this report is on active detection techniques which are based on using a tunable Fabry–Perot interferometer. Active detection technique usually involve tracking, scanning or modulating mechanisms to monitor Bragg wavelength shifts. In general although the active detection schemes require more complex systems compared to the passive detection schemes, they show a better resolution [6]. In the next section we will explain the interrogation scheme which is based on Fabry–Perot interferometer.

2.4 Fabry–Perot Interferometers

Fabry–Perot interferometer (FPI) consists of two partially reflecting surfaces with a spatial separation. When a light is incident on this cavity, due to multiple reflection inside the cavity and interference of the multiply reflected lights, the transmittance of light through this cavity has a periodic characteristic with the variation of optical frequency or the spacing between the two reflecting surfaces.

Mathematical analysis of FPI has already been developed. In this section general expression for the reflectance and transmittance of a FPI will be discussed [6]. The individual mirrors in the FPI can be characterized by transmittance T_i and reflectance R_i for $i = 1, 2$ such that $R_i + T_i = 1$. Figure 2.5 shows a schematic of FPI interior structure. The excess loss which corresponds to the portion of the

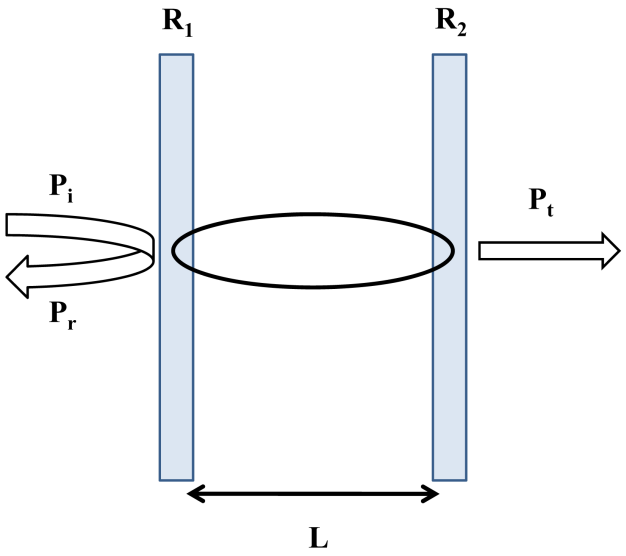

Figure 2.5: Illustration of a Fabry–Perot interferometer

incident power absorbed or scattered out of the beam by the mirror is neglected in this analysis. The Fabry-Perot reflectance R_{FP} and transmittance T_{FP} are found to be:

$$R_{FP} = \frac{R_1 + R_2 + 2\sqrt{R_1 R_2}\cos(\varphi)}{1 + R_1 R_2 + 2\sqrt{R_1 R_2}\cos(\varphi)} \tag{2.8}$$

$$T_{FP} = \frac{T_1 T_2}{1 + R_1 R_2 + 2\sqrt{R_1 R_2}\cos(\varphi)} \tag{2.9}$$

where R_{FP} represents the ratio of the power reflected by the FPI, P_r, to the incident power, P_i, T_{FP} is the ratio of the transmitted power, P_t to the incident power and φ the round trip propagation phase shift in the interferometer, is given by:

$$\varphi = \frac{4\pi n L}{\lambda} \tag{2.10}$$

with n the refractive index of the region between the mirrors and λ the free space optical wavelength. It has been assumed that the light experiences a $\pi/2$ phase shift at each reflection, as appropriate for dielectric mirrors, which is added to the propagation phase shift of φ equation.

It is evident that T_{FP} is a maximum for $\cos(\varphi) = -1$ or $\varphi = (2m+1)\pi$, with m an integer. If we define $\Delta = \varphi - (2m+1)\pi$, then near a maximum in T_{FP}, $\cos(\varphi) \approx -(1 - \Delta^2/2)$, with $\Delta \ll 1$. In the case that the mirror reflectivity are equal and approach unity, T_{FP} can be simplified to:

$$T_{FP} = \frac{T^2}{(1-R)^2 + R\Delta^2} \tag{2.11}$$

where $R = R_1 = R_2$ and $T = 1 - R$. The maximum transmittance occurs when $\Delta = 0$. The finesse F, a frequently used figure for the Fabry–Perot interferometer is defined as the ratio of the phase change between adjacent transmittance peaks to the phase change between half maximum points of either side of the peak. It is obvious that T_{FP} is a periodic function of φ with a period of 2π, so that a phase change of 2π radians is required to tune from one peak to the next. But it follows from the simplified form of T_{FP} that for high reflectance mirrors, T_{FP} is half its maximum value for $\Delta = \pm(1-R)/\sqrt{R}$. This implies that the finesse can be written as

$$F = \pi\sqrt{R}/(1-R) \tag{2.12}$$

thus in an interferometer with lossless mirrors, $F = 29.8$ for $R = 0.9$ and $F = 312.6$ for $R = 0.99$.

Another extreme case where the mirror reflectance is low ($R \ll 1$) is of particular interest in the case of fiber Fabry–Perot sensors. Assuming once again that the mirrors have equal reflectance, with $R = R_1 = R_2$ and ($R \ll 1$), we can derive the following equations:

$$R_{FP} \cong 2R(1 + \cos(\varphi)) \tag{2.13}$$

$$T_{FP} \cong 1 - 2R(1 + \cos(\varphi)) \tag{2.14}$$

It should be noted that the concept of finesses is not intended to apply to Fabry–Perot interferometers with $R \ll 1$. In fact, it follows from our definition of finesse and T_{FP} that $F = 1$ for $R = 0.172$ and F is undefined for $R < 0.172$.

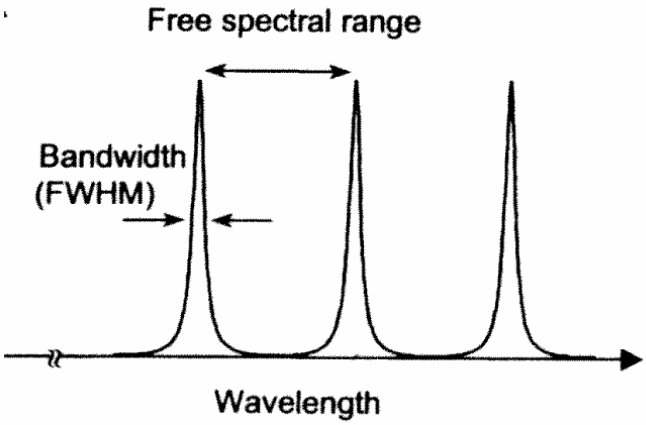

Figure 2.6: Transmittance versus wavelength of a Fabry–Perot interferometer.

Unlike other type of interferometers that are used for sensing, the FPI contains no fiber couplers–components that can complicate the sensor's deployment and the interpretation of data. The fiber FPI is an ideal transducer for many smart structure sensing applications. For an optical wave which is partially reflected by the surfaces, the extra phase it experiences during each round trip is given by:

$$\varphi = 2\pi \frac{2nl}{\lambda} + \varphi_0 \tag{2.15}$$

where n is the refractive index of the cavity material, l is the cavity length, λ is the wavelength in free space and φ_0 is the phase that might come from the reflections at both ends of the cavity (0 or 2π). If the phase difference is a multiple of 2π radians, then the transmittance becomes maximum due to the constructive interference. Figure 2.6 shows a typical transmittance versus wavelength plot for a regular Fabry–Perot interferometer.

The transmittance curve is usually plotted as a function of the cavity length or optical frequency. However the curve plotted as a function of wavelength is more useful in understanding the interrogation principle, because we usually specify a light with a wavelength rather than frequency. Although the phase difference is inversely proportional to wavelength, the small change in phase is approximately

proportional to the small change in wavelength, because $\Delta(\frac{1}{\lambda}) = -\frac{\Delta\lambda}{\lambda^2}$. Typically, tunable fiber Fabry–Perot interferometers have bandwidths of about 0.2 to 0.6 nm and a free spectral range of 4 to 60 nm and a finesse factor (which is the ratio of free spectral range to the bandwidth) of 100 to 200. Filter tuning is achieved by accurately adjusting the reflection surface separation using a piezoelectric element [6].

2.5 Fiber Grating Sensors Based upon Fabry–Perot Interferometer

Figure 2.7 shows a schematic diagram of a tunable FPI for demodulating the wavelength shift of a single fiber Bragg grating. Typically the FPI bandwidth is comparable to the grating bandwidth. The free spectral range should be larger than the operating range of the grating to avoid measurement ambiguity.

The closed–loop feedback arrangement locked the Fabry–Perot pass–band to the grating reflection signal. By the sinusoidal dithering of the cavity length of the filter, the filter transmission wavelength is periodically changed by a fraction of its pass-band. If the resonance wavelength of the filter matches the reflection wavelength of the fiber grating, the detected power reaches a maximum due to the maximal overlap (in the frequency space) of the filter pass–band and the grating reflection spectrum. If the pass–band shifts to longer or shorter wavelengths by dithering, the detected power becomes smaller. Therefore if the pass–band maximally overlaps the fiber grating reflection peak, even with dithering the cavity length of the interferometer and the received power doesn't have a varying component with the same frequency of the dithered signal. Rather it has a second order harmonic component. The first order harmonic component however exists when the filter resonance wavelength and grating Bragg wavelength do not precisely match, i.e. the two bands partially overlap. The first harmonic component of the detected

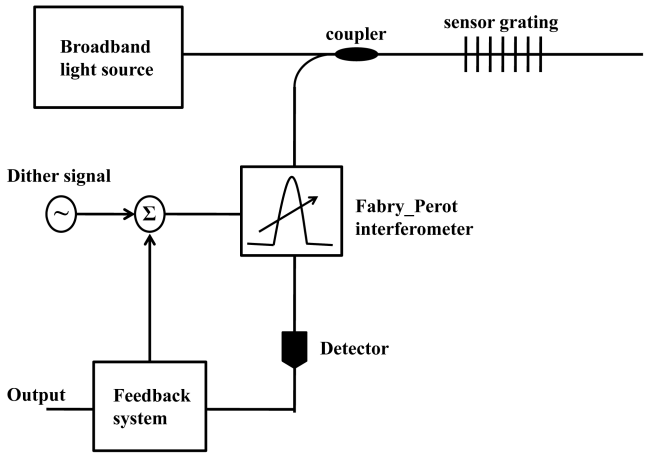

Figure 2.7: Schematic diagram of a Fabry–Perot interferometer interrogator system.

power is monitored and used as an error signal to lock the filter. The voltage applied to the piezoelectric material is used as measurement data [6].

The tracking method is applicable to a single grating sensor interrogation. Multiple grating sensor signals can be interrogated by scanning the resonance wavelength of a FPI. If the grating Bragg wavelengths and their ranges of change due to measurands do not overlap and yet fall within the spectral bandwidth of the light source and the free spectral range of the Fabry-Perot interferometer a number of gratings along the same optical fiber can be interrogated.

2.6 Fabrication of Fiber Gratings

The fiber gratings are usually fabricated by introduction of a periodic modulation of the optical properties of the fiber. This may be achieved by permanent modification of the refractive index of the core of the optical fiber or by physical deformation of the fiber [7]. The modulation of the core refractive index can be achieved by ultraviolet irradiation [8], ion implantation [9], irradiation by CO_2 lasers [10], diffusion

of dopant into the core, relaxation of mechanical stress [11] and electrical discharges [12]. One of the most widely used methods for the fabrication of fiber gratings is using UV-induced laser modulation for writing the gratings [13]. This can be done in a number of ways. One method uses two short wavelength laser beams that are angled to form an interference pattern through the side of the optical fiber. This interference pattern consists of bright and dark bands gives rise to local changes in the index of refraction in the core region of the fiber. Exposure time for making these gratings varies from minutes to hours, depending on the dopant concentration in the fiber, the wavelength used, the optical power level and the imaging optics. The refractive index modulation maybe built up on a point by point basis or the entire length of the grating may be built simultaneously by exposure of the fiber through an amplitude mask via a patterned mirror or using a micro lens array. The grating written by UV is known to contain an unstable component, which decays in time and causing a significant change in the central wavelength of the attenuation bands and in the coupling strength. This unstable component may be reduced by thermal annealing [15] and[14]. Figure 2.8 illustrate Fabrication of Long Period Grating using UV laser.

2.7 Applications of Fiber Bragg Grating Sensors

Fiber Bragg grating sensors are being developed and used in two major areas. The first is as a direct replacement for existing sensors where the fiber sensor offers significantly improved performance, reliability, safety and/or cost advantages to end users. The second area is the development and deployment of fiber Bragg grating sensors in new market areas.

One of the potential area of replacing conventional electronic sensor technologies with fiber grating senors is the area of aviation where the fiber optic sensors have the relative immunity to electromagnetic interference and are of significant weight saving and safety improvements.

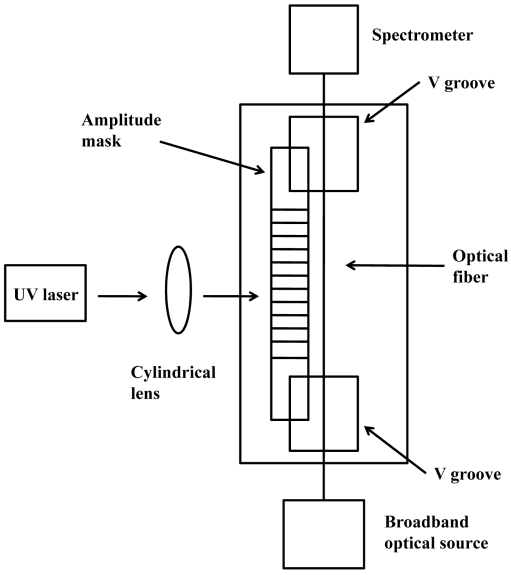

Figure 2.8: Fabrication of a Bragg grating by using UV laser

In manufacturing fiber sensors are being developed to support process control. The selling point for these sensors are improvements in environmental ruggedness and safety, especially in areas where electrical discharges could be hazardous.

The automotive industry, construction industry and other traditional sensor users remain relatively untouched by fiber sensors, mainly because of cost consideration. This can be expected to change as the improvements in optoelectronic and fiber optic communication continue to expand along with the continuing emergence of new fiber optic sensors.

Another area where the fiber sensors are mass produced is the field of medicine, where they are being used to monitor the respiratory movements in MRI [16] and skin moisture [17] and radiotherapy treatments [18]. These fiber sensors are completely passive and they pose no electrical shock threat to the patient and their inherent safety has led to a relatively rapid introduction.

Interesting areas for health and damage assessment systems are on large structures such as buildings, bridges, dams and aircrafts. In order to support these

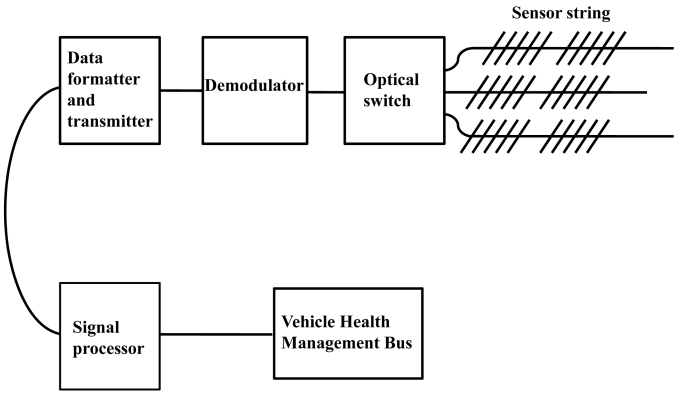

Figure 2.9: A modulator architecture for a large smart structure would consists of fiber grating sensors that are accessible through an optical switch and demodulator system that could select key sensors in each string.

type of structures, it will be necessary to ave very large number of sensors that are rapidly reconfigurable. One approach to this problem is to use fiber grating sensors that have the potential to be manufactured cheaply in very large quantities. These fiber sensors could be folded into the wavelength and time division multiplexed modulator architecture shown in figure 2.9. Here sensors are multiplexed along fiber strings and an optical switch is used to support the many strings. To avoid overloading the system the output from the sensors could be slowly scanned to determine status in a continuously updated manner.

Interesting areas for health and damage assessment systems are on large structures such as buildings, bridges, dams, aircrafts and spacecrafts. In order to support these types of structures, it will be necessary to have very large numbers of sensors that are rapidly reconfigurable and redundant.

Chapter 3

Free Spectral Range Matching Interrogation Setup

3.1 Introduction

A brief introduction on various types of interrogation techniques was given in the last chapter. In this chapter the detail of the interrogation scheme that is used for wavelength demodulation measurements will be presented.

The interrogation technique used in this research is based on using a tunable fiber Fabry–Perot interferometer (FPI). The idea is that by tuning the voltage of the FPI we match its transmission spectrum with the spectrum of fiber gratings and therefore with the wavelengths of core–core or core–cladding modes of the fiber gratings. The light coming out of a broad band source is launched into a fiber grating through a fiber coupler. The transmission (reflection) spectrum is then fed into the tunable FPI. The transmission spectrum (Fabry–Perot modes) of the FPI is tuned by applying an external DC bias. When the spectrum of FPI overlaps with that of the fiber gratings, the optical signal from the fiber gratings is selected and transmitted to the next stage. The optical signal then passes through

a multi–channel bandpass filter and split into different channels depending on the wavelength range. The signal in each channel is then detected by an InGaAs photo–detector. The data is acquired in the form of voltage through a National Instrument data acquisition card. Figure 3.1 illustrates a schematic of the Free Spectral Range Matching Interrogation (FSRMI), technique which is used in this research. In the following sections we will go through each part in detail and explain the operation of each component.

3.2 Broadband Light Source

The broad band source used for this research has a C–band spectrum in the wavelength range of 1520 to 1570 nm. The average optical intensity of this light source is -20 dBm. An Erbium Doped Fiber Amplifier (EDFA) is connected in series with the broadband light source to enhance the optical signal by 16 dBm. The output light of the EDFA is then launched into the fiber grating via an optical circulator.

3.3 Fabry–Perot Interferometer

The FSRMI technique for wavelength demodulation is based on using tunable FPI as a narrow bandpass filter. The tunable FPI is designed in such a way that each external tuning voltage allows the transmission of light at one specific wavelength. The structure of the FPI and its operation were explained in the last chapter. Two important specifications of the FPI are the linewidth of each transmission peak (Fabry–Perot mode), and the free spectral range which is defined as the distance between the transmitted wavelengths. The FPI used for this research has a model of FFP-TF2 and was purchased from Micron Optics company. It has a linewidth of 2 pm and a free spectral range of 4 nm. The free spectral range of FPI is fixed. The fineness factor which is defined as the ratio of free spectral range to bandwidth

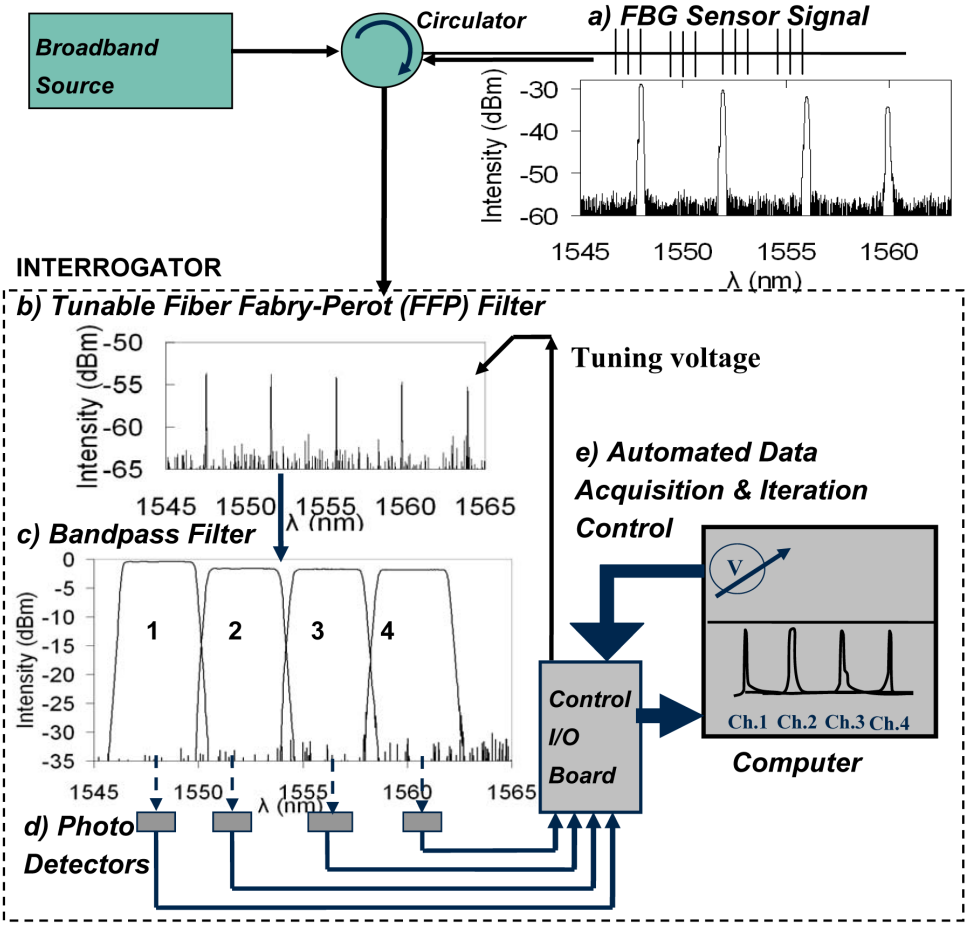

Figure 3.1: Schematic of Free–Spectral–Range–Matched–Interrogation technique, [19]

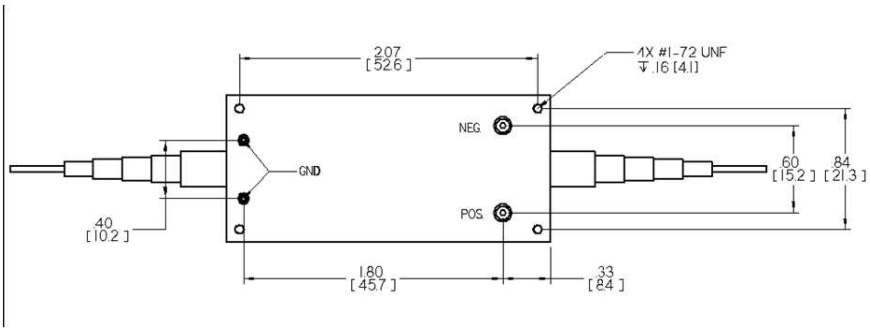

Figure 3.2: Schematic of Fabry–Perot interferometer

is 20. The measured insertion loss of the FPI is about 10 dBm. Figures 3.2 and 3.3 picture the Fabry–Perot interferometer that is used in this research and its transmission spectrum.

3.4 Calibration of FPI by Tuning the External Bias

Before running measurements the FPI needs to be calibrated. Filter tuning is achieved by changing the distance between the reflection facets of the FPI. The distance is controlled by a piezoelectric element. By changing the external DC bias that is applied to the piezoelectric one can tune this distance and the transmission peaks of FPI shift to longer or shorter wavelengths. The calibration curve of the FPI transmitted wavelength versus the tuning voltage is therefore obtained.

The calibration of FPI is carried out by a $LABview^{TM}$ program. The broad band source light is launched directly into the FPI and the transmission spectrum is detected by an optical spectrum analyzer. The tuning ports of the FPI are connected to the output of a high voltage DC voltage source which is controlled by the $LABview^{TM}$ program. The start and stop voltages and incremental steps of the external bias are preset. The LABview program increases the external voltage step by step until it reaches the stop voltage. At each voltage step a single sweep is

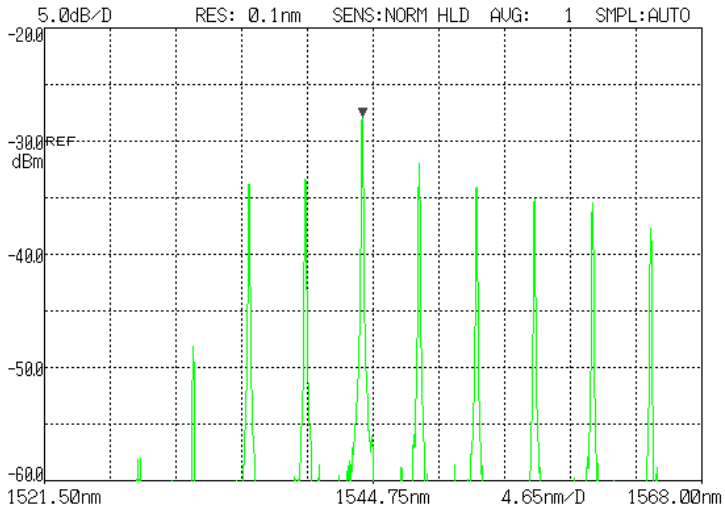

Figure 3.3: Transmission spectrum of FPI at zero bias

done by the optical spectrum analyzer and the wavelength at which the transmission peak occurs is recorded by the program.

3.5 Bandpass Filter

The bandpass filter is an optical device that allows light within a certain wavelength range to pass and attenuates light out of this range. An ideal filter has a completely flat line–width and attenuates completely all wavelengths outside the line–width. In practice the filter does not entirely block the light at wavelengths outside the transmission band range; in particular, there is a region just outside the intended line–width where wavelengths are attenuated, but not completely rejected. This is known as the filter roll–off.

The bandpass filter used in this research is a four–channel filter that is manufactured by Opto–Link. The channels cover the wavelength range of 1545.7–1562.7 nm and the line–width of each channel is 4 nm which matches the free spectral range of the FPI. The insertion loss of each channel is measured to be 10 dBm. The non-uniform transmission pattern of the four channels of bandpass filter and

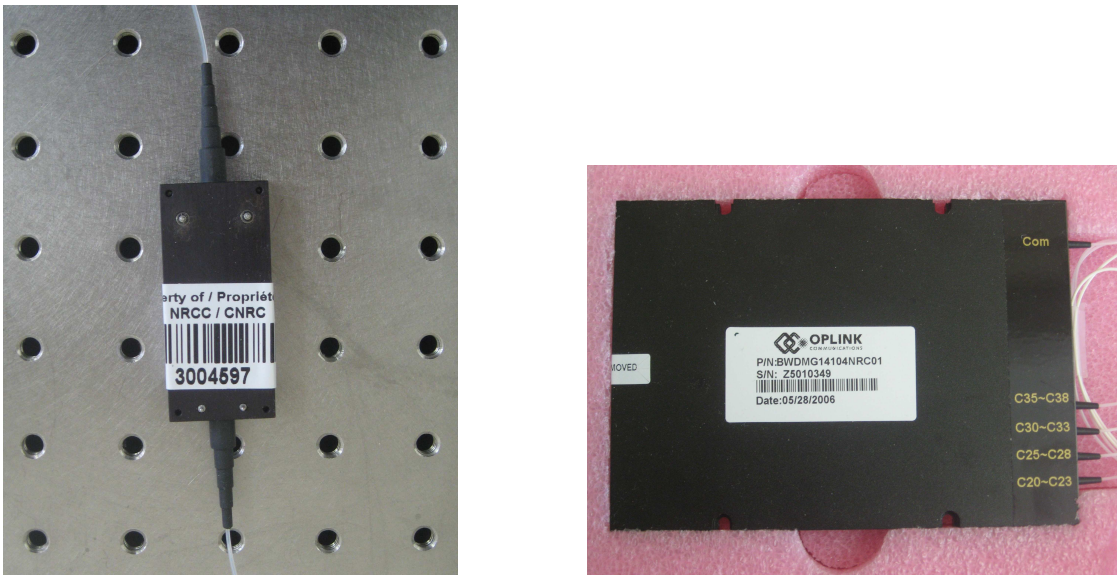

Figure 3.4: Fabry–Perot interferometer and four channel bandpass filter that are used for measurements.

the non–uniform output of the light source might result in variation of the intensity of these channels. Figure 3.4 displays the Fabry–Perot interferometer and the bandpass filter used in this research.

3.6 Photo–detectors

In order to convert the optical signals to electronic signals, four FD–InGaAs high speed photodiodes manufactured by EG & G Company are employed. They can tolerate optical power up to 1 Watt and the weakest optical signal that they can detect is 1 nW. The manufacturer responsivity is 95 %. Each of the four photo–detectors is mounted on a breadboard and is connected in series with a 1.2 $M\Omega$ load resistor. A 5 volt reverse bias is applied to the combination of a photo–detector and a load resistor.

By using a tunable laser source with an extremely narrow bandwidth the photodiodes are calibrated as a function of the light intensity and light wavelength to

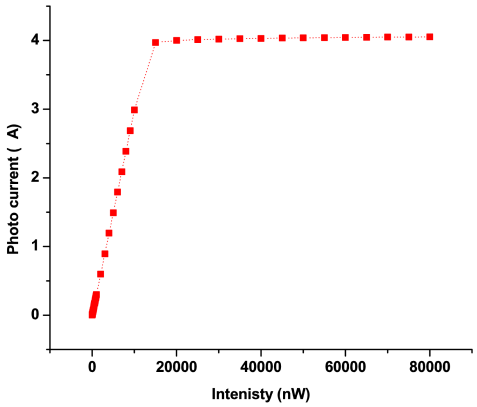

Figure 3.5: Calibration of the wavelength sensitivity of the photo–detector

verify that they all generate the same output signal under the same condition of input light intensity and wavelength. Figures 3.5 and 3.6 illustrate the intensity and wavelength calibration curves of one of the photodiodes. The photocurrent increases linearly with increasing light intensity and saturates at 16 μ watt. The output signal of the photo–detector shows slight dependence on the input light wavelengths.

3.7 Intensity of the Optical Signal

In the interrogation technique described here, the detected signal intensity (I) is proportional to the overlap among fiber grating spectrum ($R(\lambda)$), the FPI transmission pattern ($F(\lambda)$) and the bandpass filter transmission pattern ($B(\lambda)$):

$$I = \int R(\lambda)F(\lambda)B(\lambda)d\lambda \tag{3.1}$$

where $B(\lambda)$ is the normalized bandpass filter transmission, and $B(\lambda) = 1$ when $\lambda_a \leq \lambda \leq \lambda_b$ and $B(\lambda) = 0$ otherwise. The transmission spectrum of FPI, $F(\lambda)$, can be approximated as a delta function in each corresponding free spectral range

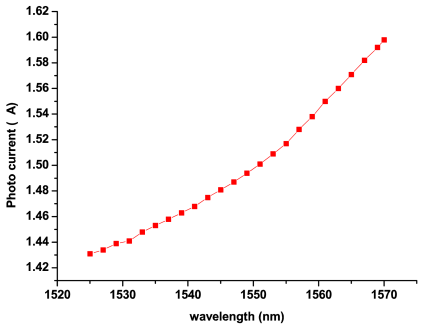

Figure 3.6: Calibration of photo–detector intensity.

[19]. The intensity of the detected signal is therefore proportional to the spectrum of the gratings, $R(\lambda)$.

$$I = \int R(\lambda).\delta(\lambda - \lambda_0).1d\lambda = R(\lambda_0) \ \lambda_a \leq \lambda \leq \lambda_b \tag{3.2}$$

3.8 Data Acquisition Setup

To collect the data a SCB–68 board which is accompanied by a Data acquisition card manufactured by National Instrument company is employed. The data acquisition card (DAQ) is a PCI-4016 model which is installed inside a personal computer. The driver used for running the DAQ card is called DAQmx. Four analogue inputs (A/I) of the board are connected to the output of the four photodiodes. The tuning voltage of the FPI can also be controlled by the analogue output (A/O) of the DAQ card within a limited range of $[-10, 10]$ V. The maximum frequency of collecting data and number of averaged samples are restricted by the type of DAQ card and is 10 kHz for the card that is used in this measurement. Figure 3.7 shows a schematic of the data acquisition setup.

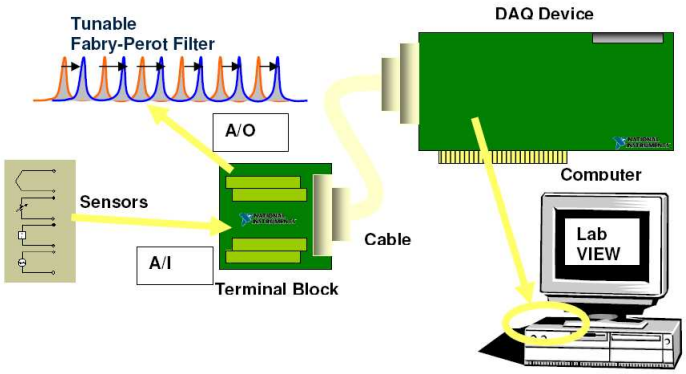

Figure 3.7: Schematic of data acquisition setup, [20]

3.9 Labview Program

The $LABview^{TM}$ program has two main steps. In the first step it tunes the external voltage applied to the FPI by a Keithly–137 DC voltage source and in the second step it goes through a loop to measure the light intensity of each photo–detector.

3.9.1 Continues Scanning and real time display and measurement

This function allows continuous data collection. The real time measurement is displayed on the screen and the scanning ends only upon termination by user. This function can also be used for tuning the voltage of FPI in case the DAQ board is being used for this purpose.

3.9.2 Tuning voltage range and incremental interval

Before iteration begins the user has to enter the maximum and minimum tuning voltage and the voltage steps. Since the accuracy of the data collected can not be

better than the accuracy of the calibration plots, the voltage steps should not be smaller than the steps used for calibrating the FPI interferometer.

3.9.3 Data collection and sample rate

Data is acquired and saved in the format of voltage drop across the load resistors. There is a feature in the labview program called DAQ assistant that allows the user to determine the sample rate and how many samples are to be taken. The higher the sample rate with more sample points the better the resolution and the slower the data acquisition will be. Furthermore one needs to take the noise-transient factor into consideration when specifying the sample rate.

Chapter 4

Results and Discussion

By using the Free Spectral Range Matching Interrogation (FSRMI) technique, we did some real time scanning and wavelength demodulation measurements on conventional Fiber Bragg Gratings (FBG), Tilted Fiber Bragg Gratings (TFBG) and Long Period Gratings (LPG). The major differences among these fiber gratings are the period and length of the conventional profile of the refractive indices of the fibers.

4.0.4 Fiber Bragg Gratings

Conventional fiber Bragg gratings (FBG) are known for reflecting light at specific wavelengths as a result of coupling between the core modes. The wavelengths of the reflected beam are strongly affected by the change of some environmental parameters such as humidity, temperature, strain along the fiber and the change in the refractive index. White light with a broadband spectrum is launched to the fiber Bragg grating sensor. Inside the FBG the optical wave is partially reflected back from each part of the gratings. The wave that is partially reflected from the gratings interferes constructively with the incoming light at a specific wavelength which is called the Bragg wavelength. Therefore only a narrow spectrum of the

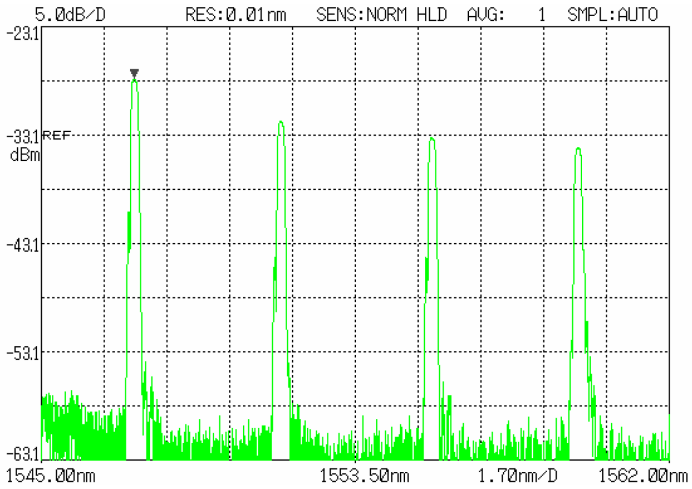

Figure 4.1: Reflection spectrum of the FBG recorded by optical spectrum analyzer with a resolution of 20 pm

broadband light is reflected while other wavelengths are transmitted through the FBG. The Bragg wavelength can be given by the following equation:

$$\lambda_B = 2n_{co}\Lambda \tag{4.1}$$

where n_{eff} is the effective refractive index of the fiber core and Λ is the grating period. The theory of coupling in fiber gratings was explained in chapter 2. Figure 4.1 shows the spectrum of the Fiber Bragg Grating recorded by the optical spectrum analyzer at room temperature and under no strain. An array of 4 wavelength division multiplexed FBG was written inside a piece of standard fiber. The FBGs are fabricated with Bragg wavelengths of 1547.520 nm (FBG1), 1551.480 nm (FBG2), 1555.570 nm (FBG3) and 1559.520 nm (FBG4) and reflectivities of approximately 70 percent. Each of the peaks can be captured within one of the channels of the bandpass filter. This wavelength separation is also the same as the free spectral range of the FPI.

4.0.5 Calibration of the Fiber Fabry-Perot Interferometer

Before using the FSRMI setup for wavelength demodulating of the FBG, the FPI needs to be calibrated. Calibration is done by remotely tuning the external voltage that is applied to FPI through a Keithly DC voltage source. Since the interrogation system would scan four different wavelength bands simultaneously, four of the transmission peaks of the FPI need to be calibrated. By tuning the voltage of the FPI, the wavelength band of each channel of the bandpass filter can be swept and the location of the reflected wavelengths of the FBG can be determined as a function of the tuning voltage.

To calibrate the FPI, an optical circuit is designed and made. The calibration is controlled and carried out by a LABview program. After setting the start and stop wavelengths and voltage values, light from a broadband source is launched into the FPI and the transmission spectrum of the FPI is fed into the OSA. The wavelength of the transmission peaks of FPI are then read directly from the OSA. Each reading is averaged out of 20 seconds of continuous sweeps of the spectrum. The values of the reflected wavelength and the external bias in each step are saved in a text file and are used later for plotting the calibration curves. It should be mentioned here that the accuracy of the calibration curves depends on the resolution of the optical spectrum analyzer while the accuracy of the measurements depends on the noise level.

– The resolution of the optical spectrum analyzer is the minimum of the spatial distance that can be distinguished. The minimum resolution with which the OSA can read the wavelength measurements is 10 pm. This means that the spectral distance between peaks must be at least 10 pm in order to be distinguished. To ensure this, one needs to verify the increment voltage of the external bias applied to the FPI is large enough to have the transmitted peak moved by more than 10 pm in each step. The voltage step used here is 0.1 V, which shifts the spectrum by about 12 pm.

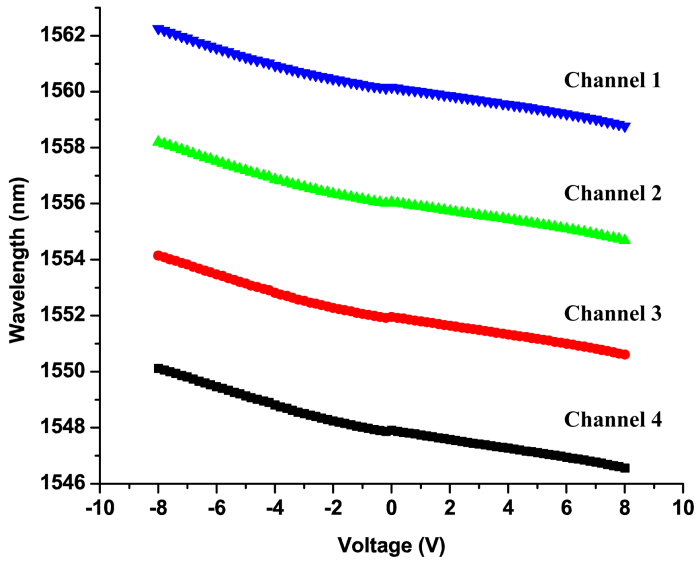

Figure 4.2: Calibration of the FPI versus tuning voltage.

Table 4.1: Fourth order polynomials that are fitted to the experimental calibration curves.

Channel1	$\lambda = 1547.86847 - 0.18038V + 0.01208V^2 - 7.25887 \times 10^{-4}V^3 - 1.26679 \times 10^{-5}V^4$
Channel2	$\lambda = 1551.92244 - 0.17184V + 0.01087V^2 - 8.50274 \times 10^{-4}V^3 - 5.6829 \times 10^{-5}V^4$
Channel3	$\lambda = 1556.01665 - 0.16411V + 0.00974V^2 - 9.37028 \times 10^{-4}V^3 - 4.56356 \times 10^{-5}V^4$
Channel4	$\lambda = 1560.12633 - 0.15693V + 0.00845V^2 - 9.99031 \times 10^{-4}V^3 - 3.40065 \times 10^{-5}V^4$

– The maximum difference between the actual and the real value of a given signal defines a parameter which is called accuracy. The optical spectrum analyzer needs to be calibrated at least once a year to ensure sufficient accuracy. Figure 4.2 illustrates the calibration of four wavelengths of FPI. The calibration plots were fitted using fourth order polynomials. The voltage was increased by 0.1 V at each step and this voltage step makes the peak shift by about the resolution limit of the OSA. Table 4.1 lists the polynomials that are fitted to the experimental calibration curves.

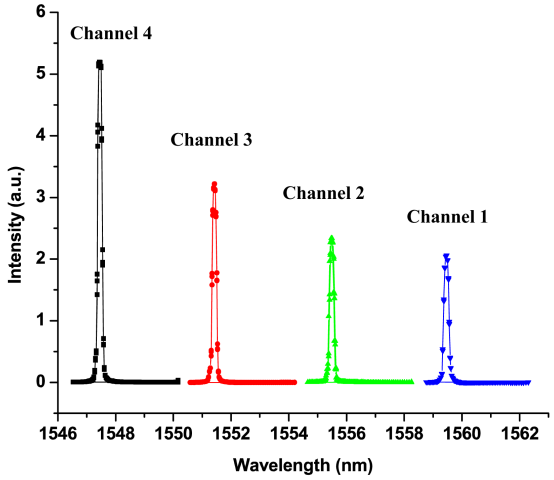

Figure 4.3: Reflection spectrum of the FBG recorded by the FSRMI interrogation technique.

4.0.6 Scanning the FBG Spectrum

Having the calibration curves of the Fabry–Perot interferometer, the FBG spectrum can be measured using the FSRMI interrogation technique. The light of the broadband source that is amplified by an EDFA is launched into a circulator and then goes through the FBG. The reflected light from the FBG is fed into the Fabry–Perot interferometer through the circulator. The FPI is sweeping the wavelength band within which the FBG peaks are located. The spectrum is then fed into the bandpass filter which splits the spectrum into 4 wavelength windows. The output signal of the bandpass filter is then converted to an electrical signal by the use of 4 photodiodes. The electrical signal of the four photodiodes in the form of voltage is then collected by a data acquisition (DAQ) card. The measured data is in the format of voltage which is proportional to the intensity of the incoming optical signal. One can then plot the intensity of the signal as a function of the tuning voltage applied to the FPI. By using the calibration curves in figure 4.2 the tuning voltage can be converted to the optical wavelength. The reflection spectrum of the FBG

Table 4.2: Gaussian functions fitted to the reflection peaks of the FBG.

Channel1	$V = 0.00807 + \frac{0.42867}{0.15349\sqrt{\pi/2}} exp(-2\frac{(\lambda - 1559.46109)^2}{0.15349^2})$
Channel2	$V = 0.0025 + \frac{0.43392}{0.13645\sqrt{\pi/2}} exp(-2\frac{(\lambda - 1555.47657)^2}{0.13645^2})$
Channel3	$V = 0.00168 + \frac{0.56119}{0.12811\sqrt{\pi/2}} exp(-2\frac{(\lambda - 1551.42392)^2}{0.12811^2})$
Channel4	$V = 0.00206 + \frac{0.96251}{0.13257\sqrt{\pi/2}} exp(-2\frac{(\lambda - 1547.45575)^2}{0.13257^2})$

(intensity vs. wavelength) can be plotted as displayed in figure 4.3. Each peak is situated within one of the channels of the bandpass filter and therefore detected by one of the photo–detectors.

In order to determine the central wavelength of the detected peak, the experimental data is fitted to a gaussian function and the center of the Gaussian function is recorded as the FBG reflection spectrum. Table 4.2 shows the gaussian functions that are employed to fit the experimental curves in figure 4.3.

From the fittings, the central wavelengths of each peak are derived as 1547.455, 1551.423, 1555.476, 1559.461 nm ±20 pm. These values can be compared to the values observed on the optical spectrum analyzer shown in figure 4.1. The central wavelengths of the peaks measured by the OSA are 1547.512, 1551.480, 1555.570, 1559.510 nm ±10 pm respectively. Taking the difference of the resolution of the OSA and FSRMI technique into account there is a difference of 40 pm between two sets of readings. This difference can be attributed to the following reasons:

−The first reason is the effect of noise. This noise has an electrical and optical origin. The electrical noise can be caused by the DAQ card and computer interface and the internal electrical noise of the OSA. This type of noise can be minimized by setting the same electrical ground for the DAQ card as for the other electrical component of the circuit (e.g. photo–detectors). The electrical noise of the OSA can be minimized by a nulling process which can be performed by running an internal function of the OSA. The optical noise can originate from the

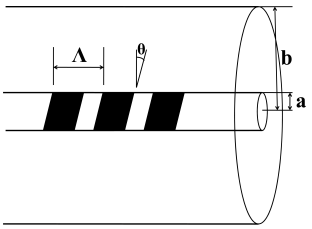

Figure 4.4: Schematic diagram of the tilted fiber Bragg gratings.

electro–optical component of the system; e.g. the Fabry–Perot interferometer and photo–detectors. We noticed that the FPI spectrum drifts gradually to the longer wavelength as we set the voltage. This small time drifting, which is of the order of 20 pm/min, can result in inaccuracy in the final readings. In order to minimize this drifting effect we decided to do the calibration and the real scanning measurements simultaneously. In order to do that, we used a coupler to split the signal of the FPI into two; one goes to the OSA and the other goes to the bandpass filter. Also the LABview programs that were used for calibrating FPI and detecting the FBG spectrum were merged into one program. So at each step when the voltage of the FPI is tuned the transmission wavelength of FPI is read by the OSA and at the same time the intensity of the transmitted light through the bandpass filter is also read. This helps to minimize or to eliminate the effect of wavelength drift of the FPI on calibration.

−The second potential source of error is from inaccuracy of the calibration. This type of inaccuracy can be improved by increasing the data points for each voltage step and averaging the data. Averaging the experimental data minimizes the effect of white noise which is dominant in single sweep operation.

−The third reason for the difference between the OSA and FSRMI readings can be due to the numerical fitting process which is negligible compared to the other reasons.

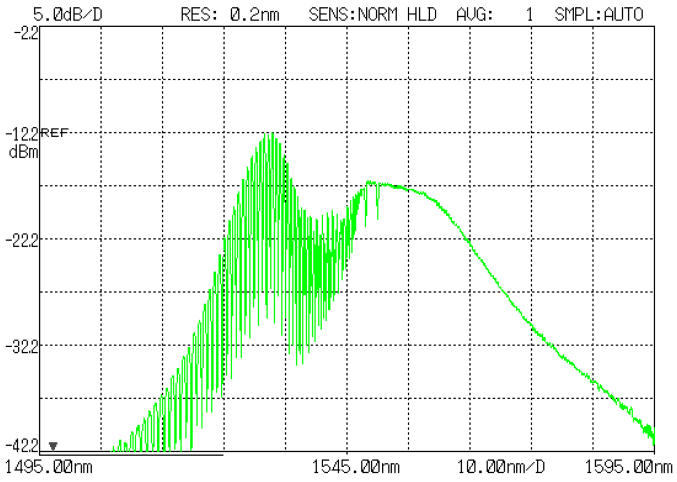

Figure 4.5: Transmission spectrum of TFBG1 under no strain and at room temperature detected by OSA.

4.1 Introduction to Tilted Fiber Bragg Gratings

Tilted Fiber Bragg Gratings (TFBG) are short period gratings (period 0.5 μm) where the core refractive index modulation is tilted with respect to the fiber axis by a certain angle as shown in figure 4.4. In single mode fibers a small tilt angle can induce coupling the core modes to the cladding modes. As a result multiple dips are present in the transmission spectrum of this type of grating. The same as FBG, the location of the dips depends on parameters such as the tilt angle [1], the refractive index of the surrounding [21] and environmental parameters such as strain, pressure and temperature [22].

TFBGs are manufactured into hydrogen-loaded Corning single mode fibers by means of a frequency doubled Argon ion laser emitting at 244 nm [22]. A 1060 nm period uniform phase mask was mounted on a rotating stage in order to apply a tilt in the plane perpendicular to the incident laser beam. The mean optical power was kept constant and the gratings were inscribed with a single sweep of the UV laser along the phase mask with a velocity of the order of 10 $\mu m/s$. After the writing process the gratings were annealed at 100 $^{\circ}C$ for a few hours.

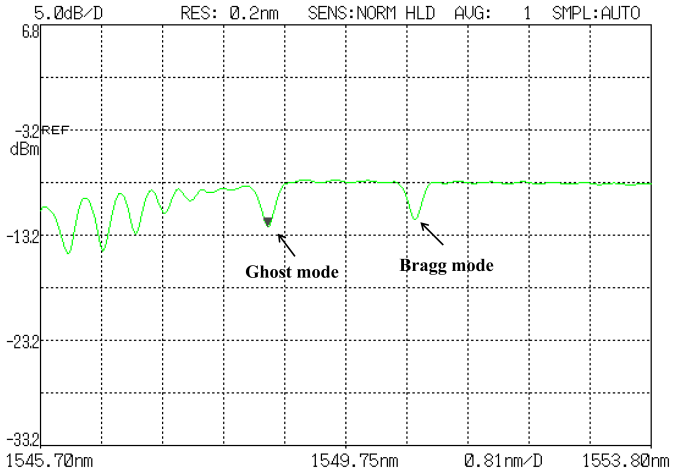

Figure 4.6: Bragg and Ghost modes of TFBG on OSA. The resolution of OSA was set on 0.1 nm.

In this section the results of using the FSRMI for interrogating the TFBG sensors will be discussed. Figure 4.5 displays the full spectrum of TFBG measured using an optical spectrum analyzer.

4.2 Spectrum of Tilted Fiber Bragg Grating

The existence of the angle in TFBG induces coupling from the core mode to azimuthally and non-azimuthally symmetric contra propagating cladding modes and to the contra propagating core modes. As a consequence multiple dips can be observed in the transmission spectrum of TFBGs. White light is launched into the TFBG and the transmission spectrum is measured using an optical spectrum analyzer as shown in figure 4.5. The resolution of the OSA is set at 10 pm. The coupling between the core and cladding modes leads to attenuation of the light at a series of wavelengths, which appears as many closely–spaced dips over the wavelength range between 1506 and 1550 nm. The coupling between the core mode and the contra propagating core mode gives rise to attenuation at a wavelength which

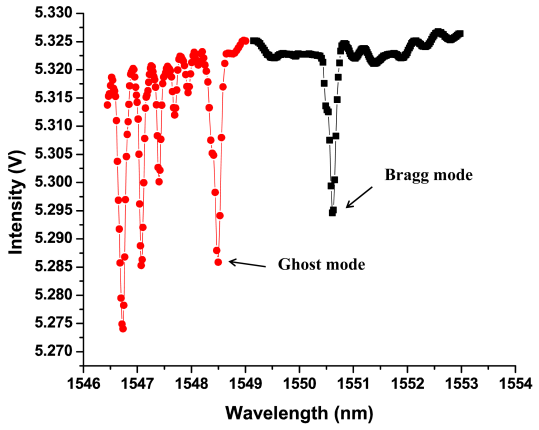

Figure 4.7: Bragg and Ghost modes of TFBG detected by FSRMI system.

is called the Bragg mode and the coupling between the core mode and the first contra–propagating cladding mode results in attenuation in a shorter wavelength which is called the Ghost mode. The location of Bragg and Ghost modes are given by the following equations:

$$\lambda_{co-co} = \frac{2n_{co}\Lambda}{\cos(\theta)} \tag{4.2}$$

$$\lambda^{m}_{co-cl} = \frac{(n_{co} + n^{m}_{cl})\Lambda}{\cos(\theta)} \tag{4.3}$$

where $n_{eff,co}$ and $n^{m}_{eff,cl}$ are the effective refractive index of the core and the m^{th} effective refractive index of the cladding and Λ and θ are the period and tilt angle of the gratings. In figure 4.6, the dip at $\lambda = 1550.606$ nm is the Bragg mode and the next prominent dip at $\lambda = 1548.497$ nm is the Ghost mode.

The Ghost and Bragg modes can be captured within the wavelength range of channels 3 and 4 of the bandpass filter of the FSRMI system. Therefore the spectrum of the Bragg and Ghost modes of the TFBG can be detected by using only two photo–detectors and two channels and thus the two corresponding transmitted wavelengths of FPI were calibrated. White light is launched into the TFBG and the transmission spectrum of TFBG is directly fed into the FPI. The transmitted light through FPI is sent to the bandpass filter, where the optical signal splits into

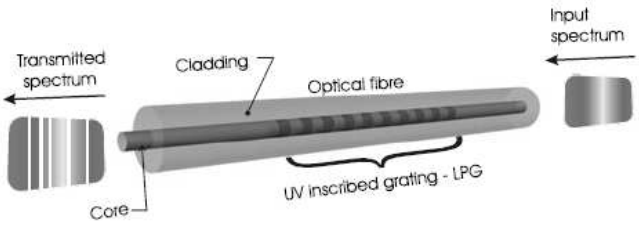

Figure 4.8: Schematic of long period grating [7]

channels 3 and 4. The spectrum of TFBG as detected by the FSRMI interrogation technique at room temperature and under no strain is displayed in figure 4.7. The peak wavelengths of the Bragg and Ghost modes detected by FSRMI are 1550.527 and 1548.387 nm ± 10 pm respectively. These numbers are obtained by fitting gaussian functions to the experimental curves of Bragg and Ghost modes.

4.3 Introduction to Long Period Gratings

Long Period Gratings (LPGs) have a period typically in the range of 100 μm to 1 mm and a length of the order of 30 mm [7], figure 4.8. The characteristics of LPGs are determined by coupling between the propagating core modes and co–propagating cladding modes. The high attenuation of the cladding modes results in a transmission spectrum of the fiber that contains a series of attenuation bands centered at discrete wavelengths. Each attenuation band corresponds to a different cladding mode. The exact form of the spectrum and the location of the attenuated wavelengths depends on factors such as period and length of the gratings as well as environmental parameters [23] and [24]. The resonant wavelengths at which the transmission spectra exhibits the minimum are approximately given by [25]:

$$\lambda^m = (n_{eff,co} - n^m_{eff,cl})\Lambda \tag{4.4}$$

where $n_{eff,co}$ and $n^m_{eff,cl}$ are the effective refractive index of core and m^{th} effective refractive index of cladding respectively [24]. The resolution of the OSA is set at 10

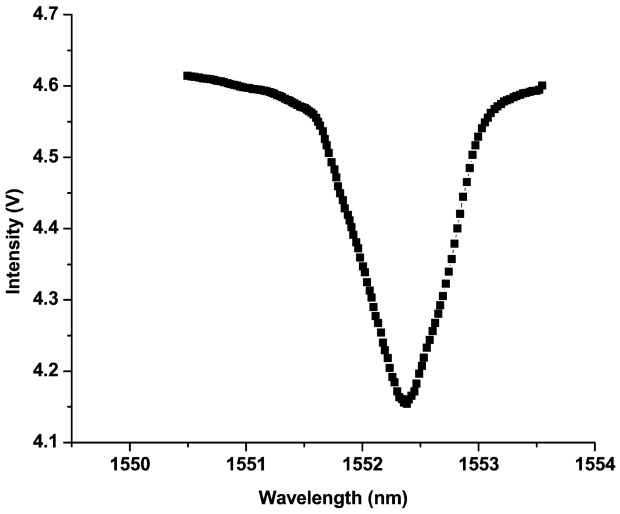

Figure 4.9: The spectrum of LPG detected by FSRMI technique.

pm. The LPG used in this research has one attenuation feature at 1544.607 nm and the attenuation is 5 dB. The spectrum of the LPG has been detected by the FSRMI technique and is shown in figure 4.9. The central wavelength of the spectrum after fitting it to a gaussian function occurs at 1552.381 nm. The wavelength accuracy of the FSRMI system is on the order of 20 pm.

4.4 Sensing Capability of the Fiber Gratings

Fiber gratings are very sensitive to variation in environmental parameters such as temperature, strain, humidity and pressure. Physical quantity changes are reflected as wavelength shift in the characteristic resonant dips or peaks of fiber gratings in the transmission or reflection spectrum [26]. The high sensitivity to variations in environmental parameters makes the fiber Bragg gratings very attractive for sensor applications. Operation as a sensor relies on the measurand–induced shift in the resonant modes. It should also be noted that bending the fiber gratings can affect the spectrum of the gratings. Therefore all strain measurements are performed when the length of the fiber that contains the gratings is stretched. In this section

the effect of temperature and strain on FBG, TFBG and LPG will be discussed.

4.5 Strain

Strain is a physical quantity that measures the deformation of an object under the effect of stress. In this study it is defined as the amount of change in the length of the fiber per unit length resulting from stretching the ends of the fiber away from each other. So it can be expressed as [27]:

$$\varepsilon = \frac{\delta l}{l_0} = \frac{l - l_0}{l_0} \tag{4.5}$$

The extension δl is positive if the length has increased and is negative if the length has decreased. So the sign of the strain is always the same as extension. Strain is a dimensionless quantity and the amount of strain is very small, it is usually measured in the unit of $\mu\varepsilon$ which is the strain that causes a 1 m long fiber to extend by 1 μm. In case of applying strain on the fiber, it is called axial or linear strain because it is only applied along one direction. In the following section the effect of axial strain on Fiber gratings will be discussed.

4.6 Effect of Variation of the Axial Strain on Gratings

4.6.1 Fiber Bragg Gratings

In order to apply axial strain to the sample, the fiber Bragg grating is fixed onto an optical table between two translation stages that have micrometer for measuring the increase of the length of the FBG. The normal length of the FBG is 650 mm.

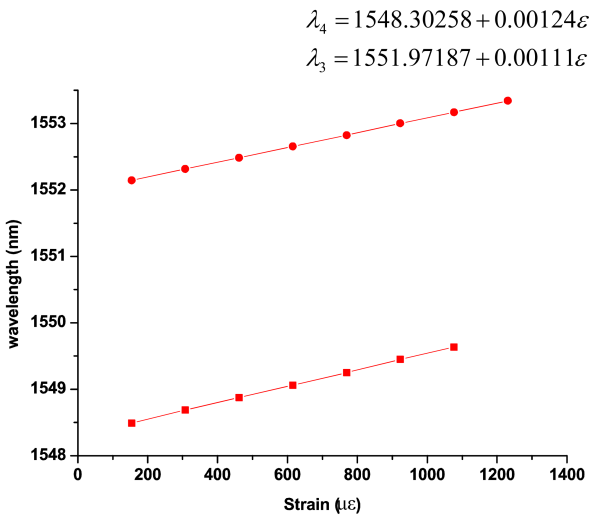

Figure 4.10: Bragg mode of FBG moves to longer wavelength linearly with increasing the strain, the plot is fitted to a linear function.

The strain variation measurements are performed at room temperature. Since the spectral resolution by which the FSRMI system is calibrated is 10 pm, the strain change between each measured point is set such that the wavelength shift of the fiber gratings is on the order of 100 pm which is an order of magnitude larger than the spectral resolution of the FSRMI system. By changing the length of the fiber between the two translation stages, the strain applied to the grating changes and this change will cause the shift in the Bragg wavelength, figure 4.10. By increasing the strain on the fiber, the Bragg mode shifts to longer wavelengths [28]. The shift to the longer wavelengths can be explained by the fact that stretching the fiber results in an increase in the period of the grating, assuming the refractive index stays constant, according to equation 4.1 this results in longer Bragg wavelength.

$$\Delta\lambda_B = 2(n_{co}\Delta\lambda + \lambda\Delta n_{co}) \tag{4.6}$$

The strain sensitivity of Bragg mode of the third and fourth reflection mode of the FBG are 0.00111 and 0.00124 $nm/\mu\varepsilon$.

4.6.2 Tilted Fiber Brag Gratings

The effect of axial strain on two TFBGs with different Bragg and Ghost modes is investigated. The Bragg and Ghost modes of TFBG1 are at 1552.482 nm and 1550.536 nm and those of TFBG2 are at 1558.375 nm and 1556.852 nm. Although the general form of the transmission spectrum stays the same but different wavelength's shift can be obtained for different regions of the spectrum as a result of strain perturbation [29]. The effect of axial strain on the Bragg and Ghost modes of the TFBG1 and TFBG2 are displayed in figures 4.11 and 4.12. Within the strain range from about 100 $\mu\varepsilon$ to 1000 $\mu\varepsilon$, both modes shift linearly to longer wavelengths by increasing the axial strain. This linear behavior is confirmed by others [29] and can be justified by the fact that by applying strain to the fiber the period of the grating and the refractive index will change and this causes a shift to longer or shorter Bragg and Ghost wavelengths according to the following equations:

$$\frac{d\lambda_{co-co}}{d\varepsilon} = \frac{2n_{co}}{\cos(\theta)}\frac{d\Lambda}{d\varepsilon} + \frac{2\Lambda}{\cos(\theta)}\frac{dn_{co}}{d\varepsilon} \tag{4.7}$$

$$\frac{d\lambda^m_{co-cl}}{d\varepsilon} = \frac{(n^m_{co}+n^m_{cl})}{\cos(\theta)}\frac{d\Lambda}{d\varepsilon} + \frac{\Lambda}{\cos(\theta)}\frac{d(n^m_{co}+n^m_{cl})}{d\varepsilon} \tag{4.8}$$

where n_{co}, n^m_{co} and n^m_{cl} are the refractive index of core and core and cladding refractive indices for the m^{th} resonance [30]. The strain sensitivity coefficients of Bragg and Ghost modes of TFBG1 are 0.00113 and 0.00117 $nm/\mu\varepsilon$ and those of TFBG2 are 0.0017 and 0.00124 $nm/\mu\varepsilon$.

4.6.3 Long Period Gratings

The effect of axial strain on the LPG is also studied. The axial strain sensitivity of the LPG can be expressed by the following equation:

$$\frac{d\lambda}{d\varepsilon} = \frac{d\lambda}{d(n_{co}-n_{cl})}\left(\frac{d(n_{co}-n_{cl})}{d\varepsilon} - \frac{dn_{cl}}{d\varepsilon}\right) + \Lambda\frac{d\lambda}{\Lambda} \tag{4.9}$$

where n_{co} and n_{cl} are the refractive indices of the core and cladding respectively, Λ is the period of the grating and λ is the central wavelength of the attenuation band.

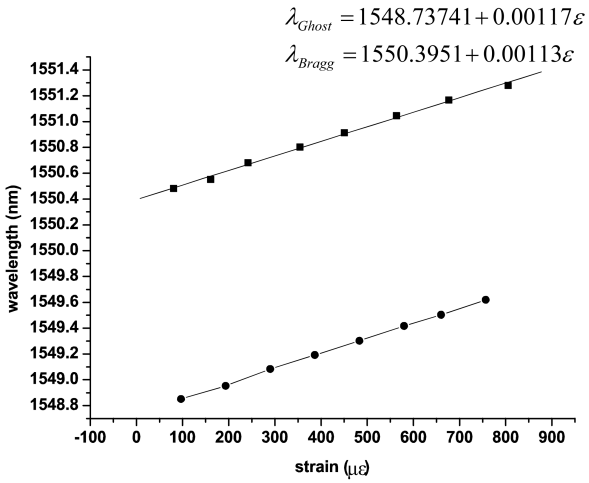

Figure 4.11: Wavelength shift of TFBG1 as a function of strain measured by FSRMI system.

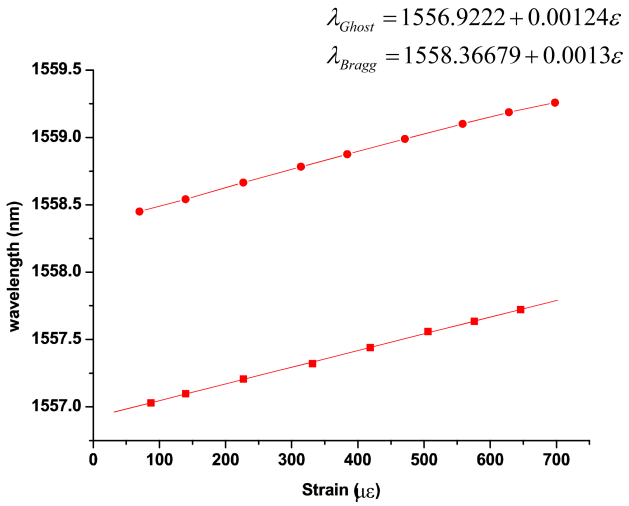

Figure 4.12: Wavelength shift of TFBG2 as a function of strain measured by FSRMI system.

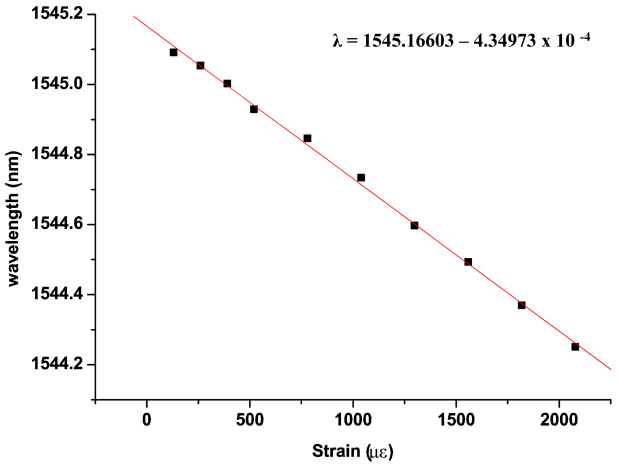

Figure 4.13: Effect of axial strain on the attenuation band of LPG.

Strain sensitivity of LPG is a result of material and waveguide effects. The material effect is caused by the change in the dimension of the fiber and and the strain optic effect, while the waveguide effect arises from the change in the period of the grating [7]. For LPG with a period $> 100\mu m$, the material contribution is negative and the waveguide contribution is positive. Appropriate choice of grating period and fiber composition will allow the generation of attenuation bands with positive, negative or zero sensitivity to strain [31]. Figure 4.13 represents the effect of strain on the attenuation band of the LPG used for this research. The attenuation band of this LPG has a negative sensitivity, $-4.34973 \times 10^{-4}\ nm/\mu\varepsilon$, to the variation of strain, thus as the strain is increased the attenuated band shifts to shorter wavelength.

4.7 Effect of Temperature Gradient on Fiber Gratings

4.7.1 Fiber Bragg Gratings

Fiber Bragg gratings respond to temperature variations by shifting their resonance modes to longer or shorter wavelengths. A number of techniques have been proposed and performed to measure the effect of temperature in the range of 20–300 K on fiber gratings [28], [32]. The sensitivity of FBG to temperature can be explained by the following equation [32]:

$$\Delta\lambda_{BT} = \lambda_B(\alpha + \xi)\Delta T \tag{4.10}$$

where $\Delta\lambda_{BT}$ is the temperature induced Bragg wavelength shift, α is the coefficient of thermal expansion and ξ is the thermo–optic coefficient. They have well-defined and positive linear responses to temperature at room temperature and above and as the temperature is reduced to liquid nitrogen temperature, thermal sensitivity has been shown to decrease nonlinearly by a factor of two and by decreasing the temperature to liquid helium temperature, it becomes approximately zero [33].

4.7.2 Long Period Gratings

The sensitivity of long period gratings to environmental parameters is influenced by a few factors such as the period of the LPG, the order of the cladding modes to which coupling takes place [8] and the composition of the fiber itself [34]. Therefore it is possible to fabricate LPGs that have positive, negative or even zero sensitivity to temperature. For many telecommunication applications spectral stability is of crucial importance and the ability to fabricate LPGs with zero sensitivity of their attenuation bands is very attractive for these applications. The temperature

sensitivity of LPG can be explained by the following equations [31]:

$$\frac{d\lambda}{dT} = \frac{d\lambda}{d(n_{co} - n_{cl}^{i})}\left(\frac{(dn_{co} - dn_{cl}^{i})}{dT} - \frac{dn_{cl}^{i}}{dT}\right) + \Lambda\frac{d\lambda}{d\Lambda}\frac{1}{L}\frac{dL}{dT} \tag{4.11}$$

where λ is the central wavelength of the attenuation band, Λ is the period of the grating and n_{co} and n_{cl} are the refractive indices of the core and cladding respectively. The first term on the right hand side arises from the thermo–optic effects. This term depends on the material composition of the fiber and the order of the cladding modes that contribute to the resonance peak. For coupling between the core and low order cladding modes, the material effect dominates. For coupling to higher order cladding modes the material effect is negligible [31]. The second term is the waveguide contribution as a result of variations in the LPG period. The magnitude and sign of this term depends on the cladding mode that couples with the core mode. $\frac{d\lambda}{d\Lambda}$ is positive for low order cladding modes and is negative for higher orders [7]. By tuning these controlling parameters, one can fabricate LPGs that have a positive, negative or zero sensitivity to temperature. At room temperature, LPG can have a linear response to temperature variations and at cryogenic temperature, this response can be nonlinear [35].

4.7.3 Tilted Fiber Bragg Gratings

The transmission spectrum of TFBG shifts with variations in temperature as well. Since the Bragg and Ghost modes are the results of core–core and core–cladding resonances, they have different sensitivities to the temperature. The shift of Bragg and Ghost modes with temperature variations can be a result of material composition of the fiber and also the order of cladding modes that couple to core mode to generate the attenuation band in the transmission spectrum. The temperature

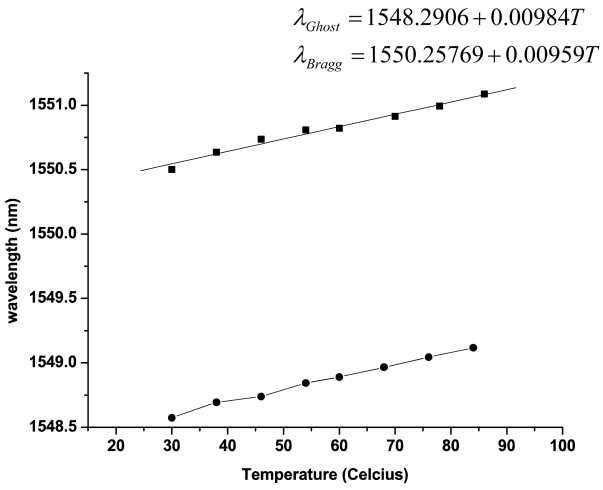

Figure 4.14: Effect of temperature on Bragg and Ghost modes of TFBG.

sensitivity of Bragg and Ghost modes can be given by the following equations [30]:

$$\frac{d\lambda_{co-co}}{dT} = \frac{2n_{co}}{\cos(\theta)}\frac{d\Lambda}{dT} + \frac{2\Lambda}{\cos(\theta)}\frac{dn_{co}}{dT} \tag{4.12}$$

$$\frac{d\lambda^m_{co-cl}}{dT} = \frac{(n^m_{co} + n^m_{cl})}{\cos(\theta)}\frac{d\Lambda}{dT} + \frac{\Lambda}{\cos(\theta)}\frac{d(n^m_{co} + n^m_{cl})}{dT} \tag{4.13}$$

In order to apply temperature gradient, we use a bicker full of water. The temperature of the water is increased in a step of 5–8 Celsius. The temperature of the TFBG in our research is tuned from room temperature to about 100 Celsius and is controlled within 1 Celsius at each set point during the measurements. The temperature steps are chosen in such a way that the wavelength shift at each point is one order of magnitude larger than the smallest wavelength resolution of the system. The temperature sensitivity measurements are performed under zero strain and on the Bragg and Ghost modes of the TFBG grating. Figure 4.14 shows the shift of Bragg and Ghost modes versus temperature gradient. Both curves show a fairly linear dependence between the wavelength shift and the temperature increase. This is attributed to the linear thermal expansion of the fiber since the grating period, Λ, increases linearly with temperature. The temperature sensitivity of Bragg and Ghost of TFBG are 9.59 $pm/celcius$ and 9.84 $pm/celcius$ respectively [36].

In summary, the FSRMI system is capable of discriminating a wavelength shift of 5 pm when the Fabry–Perot interferometer is set to have a tuning voltage with an incremental step of 0.02 V. As a result, the minimum temperature variation and strain variation that can be distinguished by the integrated FSRMI–TFBG system is estimated to be 0.5 Celsius and 0.5 $\mu\varepsilon$ respectively. This level of sensitivity is sufficient for practical applications in many environmental monitoring and structural stability studies.

Chapter 5

Conclusion

In this research we have presented a novel method for interrogating fiber Bragg grating sensors. In this method that is called "Free Spectral Range Matched Interrogation", a high finesse linewidth and tunable Fabry–Perot interferometer is employed. An multi–channel bandpass filter that has corresponding bandwidth to scanning range is used in combination with the interferometer. The high finesse linewidth of the Fabry–Perot bandpass filter and the multi–channel bandpass filter ensures a resolution of the order of 10 pm and a high responsive detection rate which is n times faster than the traditional approach, where n is the number of channels of bandpass filter. By employing a high–speed control and data acquisition system, one can expect to achieve sub-second speed of wavelength scanning. This interrogation system can be integrated with fiber Bragg gratings and can be used either in wavelength tracking mode for addressing a single sensor element in great detail with high resolution or in a fast scanning mode for addressing an array of elements.

We integrated this system with three different types of fiber ratings, fiber Bragg gratings, long period gratings and tilted fiber Bragg gratings. In each case we observed a 10 pm resolution for the fast scanning mode and a high scan speed of the order of second for scanning 16 nm wavelength range. Temperature and strain

sensitivity measurements are performed by integrating the interrogation system with the fiber gratings and the coefficient of strain and temperature sensitivity of the gratings are calculated in each case.

This interrogation system can also be integrated with the hybrid of LPG and FBG. This combination can be used for simultaneously sensing two environmental parameters. The resolution of our interrogation system is high enough to detect the changes in the spectrum of both LPG and FBG simultaneously. Applications of this hybrid device can be in DNA bio-sensing in aqueous solution where the effects of multiple parameters on the sample are studied. This type of sensing devices can also be applied to environmental studies for measuring the level of the pollution and humidity.

References

[1] R. Suo, X. Chen, K. Zhou, L. Zhang, I. Bennion, B. Liu, "Tilted fibre Bragg grating based 800 nm WDM interrogation system for strain, temperature and refractive index sensing", Proceedings of SPIE, Vol 6619, 66192(N), 2007

[2] T. Venugopalan, T. L. Yeo, T. Sun and K.T.V. Grattan, "LPG based PVA coated sensor for relative humidity measurements", Proceedings of SPIE Vol. 6619 (2007), 661925

[3] T. Erdogan, "Cladding-mode resonances in short and long -period fiber grating filters", J. Optical Soc. Amer. A, Vol. 1 (1997), pp 1760-1773

[4] T. Erdogan, "Fiber grating spectra", J. Lightwave Technol. Vol. 15 (1997), 1277-1294

[5] A. Yariv and P. Yeh, "Optical waves in crystals", John Wiley and Sons, New York, 1984

[6] Francis T. S. yu and Shizhuo Yin, "Fiber optic senosrs", Marcel Dekker, Inc., 2002

[7] Stephen W. James and Ralph P. Tatam, "Optical fiber long period grating sensors: characteristic and application", Meas. Sci. Technol. Vol. 14 (2003) R49-R61

[8] V. Bhatia and A. M. Vengsarkar, "Optical fiber long period grating sensors", Opt. Lett., Vol. 21 (1996), 692-694

[9] M. Fujumaki, Y. Ohki, J. L. Brebner and S. Roorda, "Fabrication of long period optical fiber gratings by use of ion implantation", Opt. Lett., Vol. 25 (2000), 88-90

[10] D. D. Davis, T. K. Gaylord, E. N. Glytsis, S. G. Kosinski, S. C. Metller and A. M. Vengsarkar, "Long Period Fiber Grating Fabrication with focused CO_2 laser beams", Electron Lett., Vol. 34 (1998), 302-303

[11] C. S. Kim, Y. Han, B. H. Lee, W. T. Han, U. C. Peak and Y. Chung, "Induction of the refractive index change in B-doped optical fibers through relaxation of the mechanical stress", Opt. Commun., Vol. 185 (2000), 337-342

[12] G. Rego, O. Okhotnikov, E. Dianov and V. Solimov, "High temperature stability of long period fiber gratings using an electric arc", J. Lightwave Technol., Vol. 19 (2001), 1574-1579

[13] I. Bennion, J. A. R. Williams, L. Zhang, K. Sudgen and N. Doran, "UV-written in fiber Bragg gratings", Ot. Quantum Electron., Vol. 28 (1996), 93-135

[14] P. J. Lemaire, R. M. Atkins, V. Mizrahiu and W. A. Reed, "High Pressure H_2–loading as a technique for achieving ultrahigh UV photosensitivity and thermal sensitivity in GeO_2 doped optical fibers", Electron. Lett., Vol. 29 (1993), 1191-1193

[15] D. L. Williams, B. J. Ainslie, J. R. Armitage, R. Kashyap and R. Campbell, "Enhanced UV photosensitivity in Boron co-doped germano-silicate fibers", Electron. Lett., Vol. 29 (1993), 45-47

[16] A. Grillet, D. Kinet, J. Witt, M. Schkar, K. Krebber, F. Pirotte and A. Depre, "Optical fiber sensors embedded into medical textiles for monitoring of respiratory movements in MRI environment", Prodeedings of SPIE, Vol 6619 (2007), 66191R

[17] J. Vaughan, C. Woodyatt and P. J. Scully, "Polymer optical fiber sensor to monitor skin moisture", Prodeedings of SPIE, Vol. 6619 (2007), 66191T

[18] S. Magne, L. Ager, A. Isambert, A. Bridier, P. Ferdinand and J. Barthe, "Multi-channel fiber optic dosimeter based on optically stimulated luminescence for dose verification during radiotherapy treatments", Prodeedings of SPIE, Vol. 6619 (2007), 66191N

[19] P. Tsai, Fengguo Sun, Gaozhi Xiao, Zhiyi Zhang, Somayyeh Rahimi and Dayan Ban, "A new fiber Bragg grating sensor interrogation system deploying free spectral range matching scheme with high precision and fast detection rate", IEEE Photonics Technology Letters, Vol. 20 (2008), 4, 1041–1043

[20] P. Tsai, "Free spectral range matched interrogation Technique", Unpublished report, 2007

[21] C. Caucheteur and P. Megret, "Demodulation Technique for Weakly Tilted Fibre Bragg Grating Refractometer", IEEE Photonics Technology Letters, Vol. 17, No. 12, 2703-2705, 2005

[22] D. Paladino, P. Pilla, A. Cutolo, S. Campopiano, M. Giordano, A. Cusano, C. Caucheteur and P. Megret, "Effect of Thickness and External Refractive Index in Coated Tilted iber Bragg Gratings", SPIE, Vol. 6619, 66192X, 2007

[23] V. Bhatia, "Applications of long period gratings to single and multi–parameter sensing", Opt. Expree. Vol. 4, 457–466

[24] P. Pilla, A. Cusano, A. Cutolo, M. Giordano, M. L. Korwin–Pawlowski, W. J. Bock, "Nanocoating Effect on Tapered Long Period Fiber Gratings", Proceedings of SPIE, Vol. 6619 (2007), 66192P

[25] T. Venugopalan, T. L. Yeo, T. Sun and K. T. V. Grattan, "LPG based PVA coated sensor for relative humidity measurement", Proceedings of SPIE, Vol. 6619 (2007), 661925

[26] C. Chiang, C. Shin and S. Liaw, "An intensity modulation based high–speed and high–resolution long–period fiber grating sensor interrogation system", Proc. of SPIE, Vol. 6377, 63770W (2006)

[27] E. H. Dill, "Continuum Mechanics: Elasticity, Plasticity, Viscoelasticity", CRC Press 2006

[28] S. W. James, R. P. Tatam, A. Twin, M. Morgan and P. Noonan, "Strain response of fiber Bragg grating sensors at cryogenics temperature", Measurement scienece and technology, Vol. 13 (2002), 1535-1539

[29] c. caucheteur, C. Chen, J. Albert and P. Megret, "Use of weakly tilted fiber Bragg gratings for strain sensing perposes", Procedeeings Symposium, IEEE/LEOS Benelux Chapter 2006, Eindhoven

[30] C. Chen, C. Caucheteur, P. Megret and J. Albert, "The sensitivity characteristic of tilted fiber Bragg grating sensors with different cladding thickness", Meas. Scie. Technol., Vol. 18 (2007), 3117-3122

[31] V. Bhatia, D. K. Campbell, D. Sherr, T. G. D'Alberto, N. A. Zabaronick, G. A. Ten Eyck, K. A. Murphy, R. O. Claus, "Temperature–insensitive and strain–insensitive long period grating sensors for smart structures", Opt. Eng., Vol. 36 (1997), 1872-6

[32] A. Orthnos and K. Kali, "Fiber Bragg Gratings: fundamentals and applications in telecommunication and sensing", London Artech House Publishers, London 1999

[33] M. B. Reid and M. Ozcan, "Temperature dependence of fiber optic Bragg gratings at low temperatures", Opt. Eng., Vol. 37 (1998), 237-240

[34] K. Shima, K. Himeno, T. Sakai, S. Okude and A. Wada, "A novel temperature insesnsitive long period grating using a boron–codoped germanosilicate core fiber", Tech. Dig. OFC, Vol. 97, 347-348

[35] S. W. James, R. P.tatam, R. Bateman, A. twin and P. Noonan, "Cryogenic temperature response of fiber optic long period gratings", Ellectron. Letter, Vol. 14 (2003), Iss. 8, pp 1409-1411

[36] Somayyeh Rahimi, Dayan Ban, Gaozhi Xiao and Zhiyi Zhang, "Tilted fiber Bragg grating sensors integrated with a free spectral range matched interrogation system for simultaneously real time temperature and strain monitoring", Accpeted by IEEE Sensors Journal, January 2009